Theoretical spatio-temporal analysis of angle of arrival induced by atmospheric turbulence as observed with the Grating Scale Monitor experiment

Remy Avila*, Aziz Ziad, Julien Borgnino, François Martin, Abdelkrim Agabi
Unité Mixte de Recherche 6525 Astrophysique,
Université de Nice-Sophia Antipolis - Centre National de la Recherche Scientifique,
Parc Valrose, 06108 Nice Cedex 2, France
**On leave from Instituto de Astronomía, UNAM,*
Apdo. Postal 70-264, 04510 México D.F., México

Andrey Tokovinin
Sternberg Astronomical Institute, Universitetsky prosp. 13,
119899, Moscow,Russia

Theoretical investigations of the statistical properties of the wavefront perturbed by atmospheric turbulence are presented. They are deduced from the calculation of the 2-dimensional spatial covariance and the temporal cross-spectrum of the angle of arrival fluctuations with a finite outer scale over a pair of circular pupils as in the case of the Grating Scale Monitor (GSM), or any other Shack-Hartmann type sensor. Both calculations lead to integral expressions that are numerically evaluated, and hold for any baseline vector in the mean wavefront plane. It is proposed to retrieve the wavefront outer scale $\mathcal{L}_0$ from estimations of this 2-dimensional spatial covariance, normalized by the angle of arrival structure function. In order to eliminate instrument vibration errors, the covariance and the structure function are estimated from measurements obtained by mechanically independent and mechanically coupled devices respectively. The angle of arrival temporal cross-spectrum is calculated for any mean wind velocity vector. It is shown that the baseline component in the mean wind direction affects the phase of the angle of arrival temporal cross-spectrum, while the component in the perpendicular direction affects the modulus. From simultaneous measurements of the phase of the angle of arrival temporal cross-spectrum obtained with 2 non-parallel baselines, one can calculate the mean wind speed and direction, which allows estimation of the coherence time for techniques of optical observation at high angular resolution through the atmosphere.

1. INTRODUCTION

The size of an astronomical long-exposure image depends on a single turbulence parameter, the Fried parameter r_0. However, High Angular Resolution techniques in the optical and infrared domains, namely stellar interferometry and adaptive optics, require a better understanding of the optical effects of the atmospheric turbulence. Their performances depend on spatio-temporal and spatio-angular coherence properties of the resultant wavefront on the ground. With the development of long-baseline interferometry and the increase of telescope diameters, evidence of departure from standard Kolmogorov theory for long baselines has been collected.

One of the most important effects that appears when going to long baselines is that related to the *spatial coherence outer scale* $\mathcal{L}_0$[1] of the wavefront reaching the telescope(s) (also called *wavefront outer scale*). At distances r comparable to $\mathcal{L}_0$ the spatial structure function of the phase fluctuations no longer increases as $r^{5/3}$ but begins to saturate. $\mathcal{L}_0$ can be interpreted as some weighted mean of the local optical turbulence outer scale $L_0(h)$, the weighting factor being the refractive index structure constant profile $C_n^2(h)$[1]. *In situ* measurements[2,3] have given very small local outer scales ($L_0(h) \leq$ 5m, for h $\geq$ 2km), which agrees with the repeatedly confirmed thin optical turbulence layers[4−8] and their formation mechanism recently proposed[8]. The *wavefront outer scale* $\mathcal{L}_0$ has also been estimated directly on the ground. Table 1 summarizes the available measurements which can be divided into 4 categories: integrated outer scale from *in situ* soundings, interferometric techniques, Shack-Hartmann-kind techniques with a single telescope, and Shack-Hartmann-kind techniques with multiple telescopes. As can be seen, the reported values of $\mathcal{L}_0$ are somewhat controversial. They will be further discussed in Section 5.

We give here a non-exhaustive list of consequences of a few meter outer scale, compared to an infinite outer scale model, for long-baseline interferometry, and adaptive optics: Buscher *et al.*[15] mentioned that the uncertainty in the white-light fringe position would very much decrease, making blind-pointed observations practicable in long-baseline interferometry, and that its astrometric capabilities would be improved because the major error comes from the fringe position offset caused by the low spatial frequency phase perturbations that would be reduced. The spectral bandwidth and the exposure time for both techniques would be widened[24,25]. As for the spatial modal expansion of the perturbed wavefront, a lower proportion of energy would be concentrated in the low-order Zernike components of the wavefront[26−28], which would affect the design of adaptive optics systems.

The temporal behavior of the wavefront governs the temporal parameters in high angular resolution techniques, e.g. the exposure time in speckle and long baseline interferometry, limiting the magnitude of reference sources, and the temporal bandwidth of compensating systems in adaptive optics. Several authors have studied the temporal characteristics of the wavefront. Roddier *et al.*[29] proposed a theoretical formulation of the speckle life-time due to dispersion of wind velocities in multiple turbulent layers. Roddier & Lena[30] extended this work to long-baseline interferometry. Aime *et al.*[31] noticed that the speckle temporal behavior is mostly governed by image motion. Ziad[25] studied the evolution of the signal to noise ratio in high angular resolution techniques as a function of the exposure time. As mentioned above, many authors[12−17] have measured the temporal phase power spectrum by interferometric techniques. The development of adaptive optics systems has encouraged many studies of the temporal power spectra of the turbulence-induced Zernike aberrations. Roddier *et al.*[32] calculated theoretically those spectra and presented some measurements. Conan *et al.*[33] published similar theoretical calculations for any wind speed directions, and presented some data[34,35]. Voitsekhovich & Cuevas[27] studied the effect of a finite outer scale on the temporal power spectrum of image centroid motion and Zernike coefficients. Martin[36] investigated the influence of the exposure time in the Angle of Arrival (AA) variance and structure function measurements. Lopez[37] studied the statistical properties of the AA velocity. Finally, Martin *et al.*[38] presented an example of experimental AA power spectra. Every model concerning the wavefront temporal behavior is based on the Taylor hypothesis. Some of them include several turbulent layers and some don't. A brief discussion of those aspects is presented in Section 5.

Measurement	Instrument/Telescope	$\mathcal{L}_0$ (m)	Reference
	***in situ* soundings**		
Refractive index structure function	Balloons (Paranal, Chile)	2.5	Fuchs[9] 95
	Interferometry		
Phase structure function (Ph.S.F.)	I2T (Calern, France)	~ 8	Mariotti *et al.*[10] 84
	SUSI (Australia)	$5 \sim 10$	Davis *et al.*[11] 95
Ph.S.F. + Phase temporal power spectrum (Ph.T.P.S.)	mounted on WHT (Canary Ils.)	$\sim 2 \times 2\pi$	Nightingale *et al.*[12] 91
	WHT + COAST (Cambridge, UK)	∞	Hannif *et al.*[13] 94
Ph.T.P.S., single baseline	Mark III (Mt. Wilson, USA)	> 2000	Colavita *et al.*[14] 87
Ph.T.P.S. with different baselines	Mark III (Mt. Wilson, USA)	~ 30	Buscher *et al.*[15] 95
	Mark III (Mt. Wilson, USA)	~ 30	Buscher *et al.*[16] 91
	ISI (Mt. Wilson, USA)	$5 - 20$	Bester *et al.*[17] 92
Spectral decorrelation	GI2T (Calern, France)	~ 22	Berio *et al.*[18] 96
	Shack-Hartmann-kind technique with a single telescope		
AA structure function	CFH (Hawaii)	$5 - 8$	Tallon[19] 89
Zernike variances	3.6m ESO (La Silla,Chile)	~ 50	Rigault *et al.*[20] 91
AA variances	OHP (Provence, France)	$5 - 100$	Ziad *et al.*[21] 94
Tilt covariances	KECK (USA)	$16 - 80$	Takato *et al.*[22] 95
	Shack-Hartmann-kind technique with multiple telescopes		
AA covariance	G.S.M. (Calern, France)	$10 - 300$	Agabi *et al.*[23] 95

Table 1. Reported measurements of the wavefront outer scale $\mathcal{L}_0$. Nightingale *et al.*[12] used a definition of the outer scale that differs from that used in this paper (Eq. (7)) by a factor of 2π. All other $\mathcal{L}_0$ values are consistent with the definition used here.

In response to the need of systematic measurements of the optical effects of the atmospheric turbulence at long baselines, a new version of the Grating Scale Monitor (GSM)[38,23] is being developed. It consists in a Shack-Hartmann-kind technique based on independent synchronized modules allowing the measurement of the AA fluctuations, in a given direction on the sky, with 10cm diameter pupils placed at 4 points on the wavefront, with baselines varing from 14cm to several tens of meters in any direction. The spatial wavefront parameters r_0 and $\mathcal{L}_0$ are derived respectively from the spatial structure function and spatial covariances of the AA fluctuations measured with several pairs of modules. As for the temporal characteristics, we propose to compute their Temporal Cross-Spectrum (TCS). The advantage of calculating the TCS, instead of simply the temporal power spectrum, is that the TCS contains spatio-temporal information. Hence, one can obtain from the TCS both temporal and spatial characteristics, as well as the mean propagation velocity vector of the wavefront, as will be shown in this paper. Such data analysis has to be compared with the corresponding theoretical models. The previous version of GSM used only α UMi (Polaris) as light source without tracking, whereas the new version equipped with equatorial mounts can observe any star so that it can be installed everywhere in the world. This implies that all the theoretical results concerned have to be extended for any baseline direction.

In this paper we present the theoretical calculation and analysis of the AA 2-dimensional (2-D) spatial covariance (in Section 2), and TCS (in Section 4), valid for any pair of circular pupils of any Shack-Hartmann-kind AA sensor. Both results take into account a finite outer scale, and apply for any baseline in the wavefront plane. The AA TCS holds for any mean wind direction, under the "frozen turbulence" hypothesis. Applications for retrieving the parameters of interest are discussed in Section 5, as well as some more general aspects mentioned above.

2. TWO-DIMENSIONAL SPATIAL COVARIANCE OF THE ANGLE OF ARRIVAL FLUCTUATIONS

The theoretical AA covariance is currently expressed for the particular cases in which the baselines between the two pupils, are either parallel (longitudinal covariance) or perpendicular (transverse or lateral covariance) to the direction of the observed fluctuations[39,40,23]. In order to interpret experimental results obtained when observing any star, it is necessary to calculate the 2-D covariance, for any baseline direction which can vary with time. Fig. 1 gives the most general situation and presents the notations used (the velocity vector in that figure is not of any interest in this Section, it concerns Section 4). Let $\alpha(\mathbf{r}, t)$ and $\alpha(\mathbf{r}+\mathbf{B}, t)$ be the AA fluctuations, with respect to the mean AA, measured along an arbitrary x direction, at time t, averaged over circular pupils P_1 and P_2 of the same diameter D centered respectively at positions $\mathbf{r}$ and $\mathbf{r}+\mathbf{B}$. In Fig. 1, $\mathbf{r}$ is chosen null without any loss of generality as the covariance does not depend on $\mathbf{r}$ assuming that α obeys a homogeneous random process.

A. General expression

The 2-D AA covariance may be obtained from the Fourier Transform of the AA power spectrum. If λ is the wavelength and $W_\phi(f_x, f_y)$ is the power spectrum of the phase fluctuations ϕ, one can write this covariance as[40]:

$$C_\alpha(x_0, y_0) = \lambda^2 \int_{-\infty}^{+\infty} \int_{-\infty}^{+\infty} \mathrm{d}f_x \mathrm{d}f_y \; {f_x}^2 W_\phi(f_x, f_y) \exp\left[2i\pi\left(x_0 f_x + y_0 f_y\right)\right], \tag{1}$$

where f_x and f_y are spatial frequencies corresponding respectively to the direction of fluctuation x of the AA α, and the perpendicular direction y. Changing the integration variables (f_x, f_y) into polar coordinates (f, θ) leads, in the first time, to:

$$C_\alpha(x_0, y_0) = \lambda^2 \int_0^{+\infty} \mathrm{d}f \; f^{\,3} W_\phi(f) \; I(x_0, y_0, f) \tag{2}$$

where

$$I(x_0, y_0, f) = \int_0^{2\pi} \mathrm{d}\theta \;\cos^2\theta \exp\left[2i\pi f \;\left(x_0\cos\theta + y_0\sin\theta\right)\right], \tag{3}$$

and then, using (as shown in Fig. 1) $x_0 = B\cos\gamma$ and $y_0 = B\sin\gamma$, to

$$I(x_0, y_0, f) = \mathcal{I}(B, \gamma, f) = \int_0^{2\pi} \mathrm{d}\theta \;\; \cos^2\theta \exp\left[2i\pi f B \cos(\theta - \gamma)\right]. \tag{4}$$

The definition of Bessel functions of the first kind allows us to rewrite this expression as:

$$\mathcal{I}(B, \gamma, f) = \pi\left[J_0(2\pi f B) - \cos(2\gamma)\;\; J_2(2\pi f B)\right] \tag{5}$$

and Eq. (2) becomes:

$$C_\alpha(x_0, y_0) = \mathcal{C}_\alpha(B, \gamma) = \pi\lambda^2 \int_0^{+\infty} \mathrm{d}f \;\; f^{\,3} W_\phi(f)\left[J_0(2\pi f B) - \cos(2\gamma)\;\; J_2(2\pi f B)\right]. \tag{6}$$

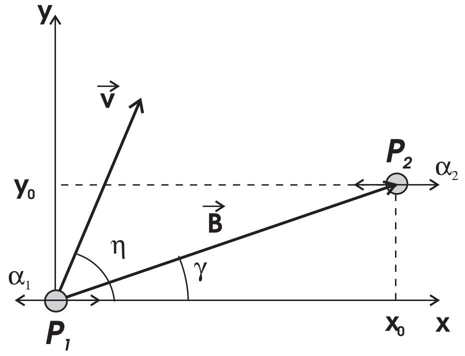

Fig. 1. General configuration for the calculation of the Angle of Arrival (AA) 2-D covariance and Temporal Cross Spectrum. α_1 and α_2 represent the AA fluctuations along x direction, measured at pupils P_1 and P_2 respectively. The baseline between both pupils has coordinates (x_0,y_0) in the cartesian system x, y, and (B,γ) in polar coordinates. The mean wind velocity with polar coordinates (v,η) is also represented.

In the framework of the so-called Von Kàrmàn model, the phase power spectrum is given by:

$$W_\phi(f) = 0.0228\; r_0^{-5/3}\left(f^{\,2} + \frac{1}{\mathcal{L}_0^2}\right)^{-11/6} \tag{7}$$

where r_0 is the Fried parameter, $\mathcal{L}_0$ is the wavefront outer scale, and where the wavefront inner scale l_0 is assumed to be equal to 0. Introducing expression (7) into Eq. (6), taking into account the spatial filtering performed by the pupils, and making explicit the dependence on $\mathcal{L}_0$ and D, the 2-D AA covariance can be written as:

$$\begin{aligned}\mathcal{C}_\alpha(B, \gamma, D, \mathcal{L}_0) = 0.0716\;\lambda^2 r_0^{-5/3} &\int_0^{+\infty} \mathrm{d}f\;\; f^{\,3}\left(f^{\,2} + \frac{1}{\mathcal{L}_0^2}\right)^{-11/6} \\ &\times\left[J_0(2\pi f B) - \cos(2\gamma)\;\; J_2(2\pi f B)\right]\left[2\frac{J_1(\pi D f)}{\pi D f}\right]^2.\end{aligned} \tag{8}$$

Substituting X for the dimensionless variable $2\pi f B$ and assuming $B \neq 0$ leads to

$$\begin{aligned}\mathcal{C}_\alpha(B, \gamma, D, \mathcal{L}_0) = 0.0388\;\lambda^2 r_0^{-5/3} B^{-1/3} &\int_0^{+\infty} \mathrm{d}X\; X^3\left(X^{\,2} + \left(\frac{2\pi B}{\mathcal{L}_0}\right)^2\right)^{-11/6} \\ &\times\left[J_0(X) - \cos(2\gamma)\;\; J_2(X)\right]\left[2\frac{J_1\left(\frac{DX}{2B}\right)}{\frac{DX}{2B}}\right]^2.\end{aligned} \tag{9}$$

The restriction on B in Eq. (9) is not troublesome, as expression (8) can be used in the case of $B = 0$ to obtain the AA variance.

Fig. 2 shows a 2-D plot of the AA 2-D covariance as a function of the baseline vector (B, γ), obtained from numerical integration of Eq. (8) for $D = 10\text{cm}, \mathcal{L}_0 = 10\text{m}$, $\lambda = 0.5\mu\text{m}$ and $r_0 = 10\text{cm}$. Only baselines with $0^o \leq \gamma \leq 180^o$ are represented. The missing half of the surface is symetrical to the plane of equation $\gamma = 0$. One can notice the smooth transition between longitudinal ($\gamma = 0^o$) and transverse ($\gamma = 90^o$) covariances.

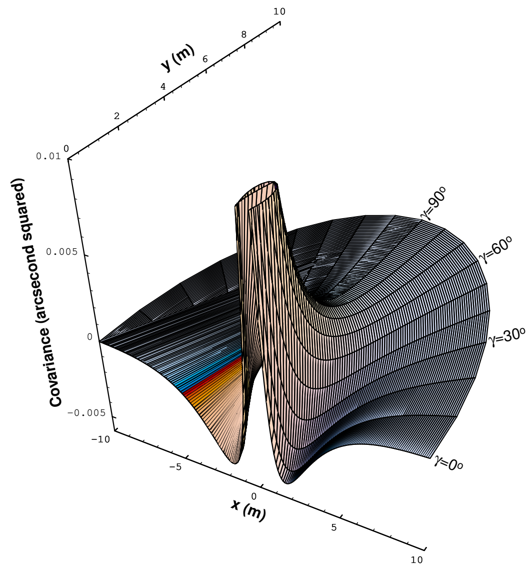

Fig. 2. 2-D plot of the angle of arrival covariance as a function of the baseline vector (B, γ), obtained from numerical integration of Eq. (8) for $D = 10\text{cm}, \mathcal{L}_0 = 10\text{m}$, $\lambda = 0.5\mu\text{m}$ and $r_0 = 10\text{cm}$. The missing half of the surface is symetrical to the one shown, with respect to the plane of equation $\gamma = 0$. Covariance values higher than 0.01 arsecond squared are not represented in order to reduce the dynamic range in the covariance axis, making visible the smooth transition from longitudinal ($\gamma = 0^o$) to transverse ($\gamma = 90^o$) covariances.

B. Particular cases

Putting $\gamma = 0$, and $\gamma = \pi/2$ we find again the longitudinal and transverse covariances respectively, as[40]:

$$\mathcal{C}_\alpha\left(B, \begin{matrix}\pi/2\\0\end{matrix}, D, \mathcal{L}_0\right) = 0.0388\ \lambda^2 r_0^{-5/3} B^{-1/3} \int_0^{+\infty} \mathrm{d}X\ X^3 \left(X^{\ 2} + \left(\frac{2\pi B}{\mathcal{L}_0}\right)^2\right)^{-11/6}$$
$$\times \left[J_0\left(X\right) \pm J_2\left(X\right)\right] \left[2\frac{J_1\left(\frac{DX}{2B}\right)}{\frac{DX}{2B}}\right]^2, \tag{10}$$

signs $-$ and $+$ correspond to $\gamma = 0$, and $\gamma = \pi/2$ respectively.

C. The distortion function

Here, let us recall that in the framework of the Kolmogorov-Tatarski model the 2-D AA covariance, without any filtering effect taken into account, is[39]:

$$C_{K_\alpha}\left(x_0, y_0\right) = 0.145\ \lambda^2 r_0^{-5/3} \left[\left(x_0^2 + y_0^2\right)^{-1/6} - \frac{1}{3} x_0^2\ \left(x_0^2 + y_0^2\right)^{-7/6}\right] \tag{11}$$

This expression is valid when the spatial shifts are contained between and very far from the limit wavefront scales l_0 and $\mathcal{L}_0$, and when the pupils are assumed infinitely small. Passing in polar coordinates, with above notations, gives:

$$\mathcal{C}_{K_\alpha}(B,\gamma) = 0.145\ \lambda^2 r_0^{-5/3} B^{-1/3} \left[1 - \frac{\cos^2\gamma}{3}\right] \tag{12}$$

One can define a "distortion function" H_{VK}, with respect to Kolmogorov-Tatarski model, as the ratio of Eqs. (9) to (12) which includes filtering effects due to the finite wavefront outer scale (for the Von Kàrmàn model) and to the finite pupil size. It can be expressed in the form:

$$\begin{aligned} H_{VK}(B,\gamma,D,\mathcal{L}_0) = & \frac{0.0388}{0.145\left(1-\frac{\cos^2\gamma}{3}\right)} \int_0^{+\infty} \mathrm{d}X\ X^3 \left(X^{\ 2} + \left(\frac{2\pi B}{\mathcal{L}_0}\right)^2\right)^{-11/6} \\ & \times \left[J_0(X) - \cos(2\gamma)\ \ J_2(X)\right] \left[2\frac{J_1\left(\frac{DX}{2B}\right)}{\frac{DX}{2B}}\right]^2 . \end{aligned} \tag{13}$$

Then, in the general case presented in Fig. 1, the 2-D AA covariance is given by:

$$\mathcal{C}_\alpha(B,\gamma,D,\mathcal{L}_0) = \mathcal{C}_{K_\alpha}(B,\gamma) \times H_{VK}(B,\gamma,D,\mathcal{L}_0). \tag{14}$$

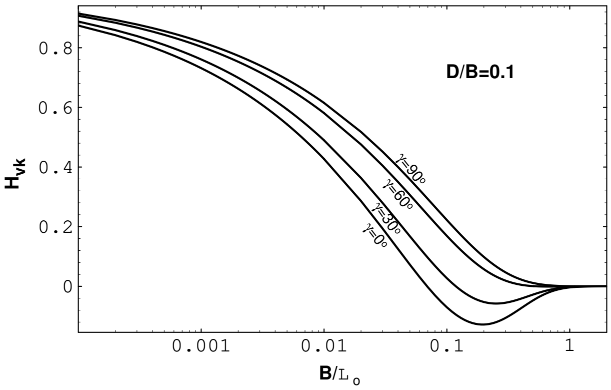

Fig. 3. Distortion function H_{VK}, obtained from numerical integration of Eq. (13) for $D/B = 0.1$ and for different values of the baseline angle γ.

Fig. 3 shows, as a function of the dimensionless variable $B/\mathcal{L}_0$, the distortion function $H_{VK}(B,\gamma,D,\mathcal{L}_0)$ for different values of the angle γ between the baseline and the direction of the AA fluctuations observed. Variations of $H_{VK}(B,\gamma,D,\mathcal{L}_0)$ between the extreme values of D/B, 0.01 and 0.2, are less than 1%. The curves are shown for the single value $D/B = 0.1$. Note the behavior of this function as γ passes from 0^o (longitudinal fluctuations) up to 90^o (transverse fluctuations). For any value of γ, the distortion function reaches 0 when $B/\mathcal{L}_0$ is close to 1. The dependence of longitudinal covariance on the baseline B and the wavefront outer scale $\mathcal{L}_0$ is presented in Fig. 4. The case of an infinite outer scale (Kolmogorov's law) also appears on the figure. There is a strong sensitivity of the covariance to the outer scale for small values of the baseline.

3. NORMALIZED COVARIANCE OF THE ANGLE OF ARRIVAL

From Eq. (8) one can obtain, putting $B = 0$, the expression for the variance of the AA fluctuations along the x-axis $\sigma_\alpha^2(D,\mathcal{L}_0)$. Moreover, the structure function is given by:

$$D_\alpha(B,\gamma,D,\mathcal{L}_0) = 2\left[\ \sigma_\alpha^2(D,\mathcal{L}_0) - \mathcal{C}_\alpha(B,\gamma,D,\mathcal{L}_0)\ \right]. \tag{15}$$

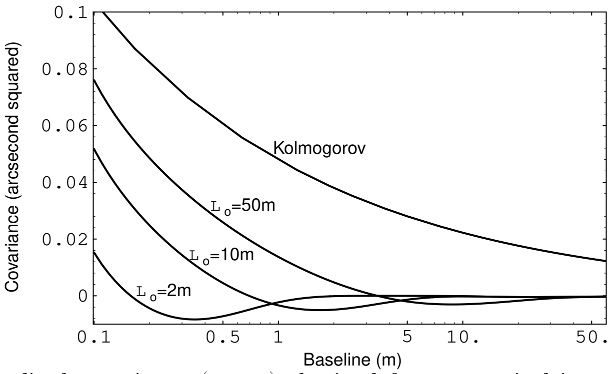

Fig. 4. Angle of arrival longitudinal covariance ($\gamma = 0$) obtained from numerical integration of Eq. (10), for $D = 10$cm, $r_0 = 10$cm at $\lambda = 0.5\mu$m, for 3 different values of the wavefront outer scale. The case of Kolmogorov's law is also presented.

A first way to normalize the 2-D AA covariance is to calculate:

$$\Gamma'_\alpha = \frac{\mathcal{C}_\alpha(B,\gamma,D,\mathcal{L}_0)}{\sigma^2_\alpha(D,\mathcal{L}_0)} \tag{16}$$

which, for a given baseline, remains a function of D and $\mathcal{L}_0$, but is no longer a function of λ nor r_0.

However, the variance $\sigma^2_\alpha(D,\mathcal{L}_0)$ is experimentally biased by possible vibrations of the telescope. To avoid this effect one can estimate r_0 in a differential way using the experiment GSM as a Differential Image Motion Monitor (DIMM), then recalculating the corresponding variance that will be thus corrected.

But, for small values of the wavefront outer scale $\mathcal{L}_0$, its effect leads to an overestimation of r_0, as stated by Borgnino *et al.*[40], and consequently to an underestimation of the calculated values of $\sigma^2_\alpha(D,\mathcal{L}_0)$.

To solve this problem, one can normalize the covariance by the structure function, given by formula (15) and measured for a small baseline (B_2,γ_2) (of the order of a few tens of centimeters). Considering that the covariance $\mathcal{C}_\alpha(B,\gamma,D,\mathcal{L}_0)$ is unaffected by vibration errors, as further discussed in section 5 A, the vibration-free normalized covariance is obtained as:

$$\Gamma_\alpha = \frac{\mathcal{C}_\alpha(B,\gamma,D,\mathcal{L}_0)}{D_\alpha(B_2,\gamma_2,D,\mathcal{L}_0)}, \tag{17}$$

from which will be deduced $\mathcal{L}_0$, knowing all other parameters.

Fig. 5 shows, for different values of the wavefront outer scale, the longitudinal covariance normalized respectively by the variance (continuous line) and by the structure function (dashed line). The curves in the first case are slightly more separated than in the second, mainly for small values of the baseline. This can be explained by the fact that the variance is more sensitive to $\mathcal{L}_0$ than the structure function[21].

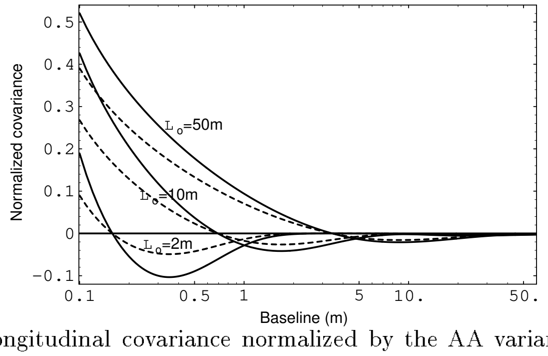

Fig. 5. Angle of Arrival (AA) longitudinal covariance normalized by the AA variance (continuous line) and by the AA structure function (dashed line) , calculated using Eq. (16) and Eq. (17) (with B_2= 0.2m, $\gamma_2 = 0^o$) respectively, for 3 different values of the wavefront outer scale, and $D = 10$cm.

4. ANGLE OF ARRIVAL TEMPORAL CROSS-SPECTRUM

A. General expression

Let $\alpha_1(t) = \alpha(\mathbf{r}, t)$ and $\alpha_2(t) = \alpha(\mathbf{r} + \mathbf{B}, t)$. Fig. 1 represents the general situation, where vector $\mathbf{v}$ is the mean wind velocity. The quantity to be calculated is the cross-spectrum of the random processes $\alpha_1(t)$ and $\alpha_2(t)$,

$$W_{\alpha,\mathbf{B}}(\nu) = \langle \widehat{\alpha}_1(\nu)\ \widehat{\alpha}_2^*(\nu) \rangle \tag{18}$$

which may be regarded as an estimation of their statistical similarity at each temporal frequency ν. The sign $\widehat{}$ indicates a Fourier transform, * a complex conjugate, and $\langle\rangle$ means an ensemble average. Throughout this paper $\alpha(\mathbf{r}, t)$ is assumed to be described by a wide-sense stationary and homogenous random process.

The temporal cross-correlation of the AA fluctuations at two positions separated by a baseline $\mathbf{B}$ is:

$$\mathfrak{C}_{\alpha,\mathbf{B}}(\tau) = \langle \alpha(\mathbf{r}, t)\ \alpha(\mathbf{r} + \mathbf{B}, t + \tau) \rangle. \tag{19}$$

Assuming that the wavefront propagates without deformation, with a velocity $\mathbf{v}$ (Taylor hypothesis in a single turbulent layer), one can write

$$\alpha(\mathbf{r} + \mathbf{B}, t + \tau) = \alpha(\mathbf{r} + \mathbf{B} - \mathbf{v}\tau, t) \tag{20}$$

No particular assumption is made on $\mathbf{v}$. It makes an angle η with the AA measuring direction considered (see Fig. 1). Substituting Eq. (20) into (19), the temporal cross-correlation reduces to the spatial covariance:

$$\begin{aligned} \mathfrak{C}_{\alpha,\mathbf{B}}(\tau) &= \langle \alpha(\mathbf{r}, t)\ \alpha(\mathbf{r} + \mathbf{B} - \mathbf{v}\tau, t) \rangle \\ &= C_\alpha(\mathbf{v}\tau - \mathbf{B}). \end{aligned} \tag{21}$$

From the Wiener-Khintchin theorem, $W_{\alpha,\mathbf{B}}(\nu)$ and $\mathfrak{C}_{\alpha,\mathbf{B}}(\tau)$ form a 1-D Fourier transform pair. Substituting $\mathfrak{C}_{\alpha,\mathbf{B}}(\tau)$ by $C_\alpha(\mathbf{v}\tau - \mathbf{B})$ in the Fourier transform, one can write

$$W_{\alpha,\mathbf{B}}(\nu) = \int_{-\infty}^{+\infty} \mathrm{d}\tau\ C_\alpha(\mathbf{v}\tau - \mathbf{B}) \exp(2i\pi\nu\tau). \tag{22}$$

The spatial covariance $C_\alpha(\mathbf{r})$ is the 2-D inverse Fourier transform of the spatial AA power spectrum $W_\alpha(\mathbf{f})$, $\mathbf{f}$ being the spatial frequency. Making explicit the Fourier transform, one can write

$$W_{\alpha,\mathbf{B}}(\nu) = \int_{-\infty}^{+\infty} \mathrm{d}\tau \left[\int\!\!\int_{-\infty}^{+\infty} \mathrm{d}\mathbf{f}\ W_\alpha(\mathbf{f}) \exp(-2i\pi\mathbf{f} \cdot (\mathbf{v}\tau - \mathbf{B})) \right] \exp(2i\pi\nu\tau). \tag{23}$$

Inverting the integration order, and rearranging the exponential arguments in order to isolate the terms that depend on τ, one can identify a delta distribution in the integral over τ, thus obtaining

$$W_{\alpha,\mathbf{B}}(\nu) = \int\!\!\int_{-\infty}^{+\infty} \mathrm{d}\mathbf{f}\ W_\alpha(\mathbf{f})\ \delta(\nu - \mathbf{v} \cdot \mathbf{f}) \exp(2i\pi\mathbf{f} \cdot \mathbf{B}). \tag{24}$$

This is a very expressive equation, analogous to Eq. (22) but now in the spatial frequency plane. The spatial 2-D power spectrum $W_\alpha(\mathbf{f})$ is cut perpendicularly to this plane along a straight line of equation $\mathbf{v} \cdot \mathbf{f} = \nu$, and a Fourier transform of the resulting 1-D function is performed. This is exactly the way $W_{\alpha,\mathbf{B}}(\nu)$ is numerically computed.

B. The case of a Von Kàrmàn model

Eq. (24) suggests that the calculation will be simplified by rotating the reference system by an angle η, in order to have one axis parallel to $\mathbf{v}$ and the other one perpendicular to it. Applying this transformation and simplifying, we obtain

$$W_{\alpha,\mathbf{B}}(\nu) = \frac{1}{v}\exp\left(2i\pi B\frac{\nu}{v}\cos(\eta-\gamma)\right)\int_{-\infty}^{+\infty}\mathrm{d}q\; W_\alpha\left(\frac{\nu}{v}\cos\eta - q\sin\eta\,,\frac{\nu}{v}\sin\eta + q\cos\eta\right)$$
$$\times\exp\left(2i\pi qB\sin(\gamma-\eta)\right). \tag{25}$$

where v and B are respectively the modulus of $\mathbf{v}$ and $\mathbf{B}$, and q represents the spatial frequency along the straight line where $W_\alpha(\mathbf{f})$ is cut, as explained above. Replacing $W_\alpha(\mathbf{f})$ by its explicit expression in the case of a Von Kàrmàn phase power spectrum (Eq. (7)) with the filtering term introduced by the pupils of diameter D, one finally gets

$$W_{\alpha,\mathbf{B}}(\nu) = 0.0228\lambda^2 r_0^{-5/3}\frac{1}{v}\exp\left(2i\pi B\frac{\nu}{v}\cos(\eta-\gamma)\right)\int_{-\infty}^{+\infty}\mathrm{d}q\;\left(\frac{\nu}{v}\cos\eta - q\sin\eta\right)^2$$
$$\times\left[\left(\frac{\nu}{v}\right)^2 + q^2 + \frac{1}{\mathcal{L}_0^2}\right]^{-11/6}\left[2\frac{J_1\left(\pi D\sqrt{\left(\frac{\nu}{v}\right)^2+q^2}\right)}{\pi D\sqrt{\left(\frac{\nu}{v}\right)^2+q^2}}\right]^2\exp\left(2i\pi qB\sin(\gamma-\eta)\right). \tag{26}$$

In order to obtain dimensionless variables and to reduce the number of independent parameters, as in the case of the 2-D AA covariance in Eq. (9), one can redefine the integration variable as $Z = qB$. However this will not be done, because the analysis of the influence of physical parameters on the TCS is simpler using Eq. (26).

C. Numerical calculation and physical analysis

TCS has been numerically calculated by means of a Fast Fourier Transform for each value of ν as suggested by Eq. (26). It also shows that $vW_{\alpha,\mathbf{B}}(\nu)$ is a function of the ratio ν/v, which reduces the number of independent variables, and indicates that any change in the wind speed translates simply as a shift of the curve of $W_{\alpha,\mathbf{B}}(\nu)$ in a log-log-plot, without changing its shape. This is why we represent in Figs. 7 to 11 modulus (a) and phases (b) of $vW_{\alpha,\mathbf{B}}(\nu)$ as a function of ν/v. They show the influence of the baseline separation B (Figs. 7 and 8), the baseline angle γ (Fig. 9), the wind direction angle η (Fig. 10) and the wavefront outer scale $\mathcal{L}_0$ (Fig. 11). All calculations were carried on considering Fried parameter $r_0 = 10cm$ at wavelength $\lambda = 0.5\mu m$ and a pupil diameter $D = 10cm$.

Before analyzing in detail the influence of each parameter , let us explain roughly what one could expect from the TCS modulus and phase. Consider the very general case described in Fig. 6. Points P_1 and P_2 denote pupil location. Dashed lines represent the perturbed wavefront reaching pupil P_1 at time t_1 and pupil P_2 at time t_2. The perturbation having crossed pupil P_1 passes through point C at time t_2 without deformation assuming the Taylor hypothesis. The baseline vector $\mathbf{B}$ (or $\overrightarrow{P_1P_2}$) can be decomposed as the sum of two orthogonal vectors $\overrightarrow{P_1C}$ in the wind direction, and $\overrightarrow{CP_2}$. The TCS modulus with baseline $\mathbf{B}$ is an estimation of the statistical resemblance of the AA measured at both pupils, in the frequency domain. But the measurement at P_1 is the same as the one that would be obtained at C after a time $t_2 - t_1$. So the TCS obtained with baseline $\mathbf{B}$ will differ from the TCS with baseline $\overrightarrow{CP_2}$ only by a phase factor. This indicates that the component of $\mathbf{B}$ in the wind direction influences only the phase of $W_{\alpha,\mathbf{B}}(\nu)$, while the component in the perpendicular direction modifies only its modulus. In order to illustrate this, Figs. 7 and 8 represent, for different values of B ($B = |\mathbf{B}|$), the TCS modulus and phases for $\eta = \gamma = 0$ (baseline in the wind direction) and $\eta = 0$, $\gamma = 90^o$ (baseline perpendicular to the wind direction) respectively. In the first case the TCS modulus is independent of B and equal to the AA power spectrum[33] which corresponds to the case $B = 0$, while its phase does depend on B, whereas in the second case the modulus depends on B, and the phase (not represented) is equal to zero for all B. A physical justification of this behavior is the following: When the baseline is parallel to the wind direction all the turbulent structures, small as well as large ones, cross each pupil with a temporal shift, provoking a linear phase term in the TCS. And as they travel without deformation, they are completely correlated when passing over each pupil, explaining that the TCS modulus remains unchanged when B

increases. If wind and baseline are not parallel to each other, only the large turbulent structures will be able to cross both pupils. The higher the angle between wind and baseline, the larger the turbulent structures that no longer pass in front of both pupils. This explains the decorrelation at high frequencies as this angle increases.

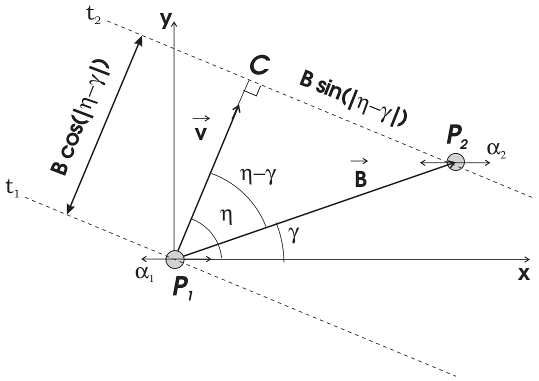

Fig. 6. Baseline components in the direction of the wind velocity, and perpendicular to it. α_1 and α_2 represent the Angle of Arrival fluctuations along x direction, measured at pupils P_1 and P_2 respectivelly. The baseline has polar coordinates (B,γ) and those of the mean wind velocity are (v,η). Dashed lines represent the perturbed wavefront reaching P_1 at time t_1 and P_2 at t_2.

Following this qualitative reasoning one can expect that the TCS phase is mainly governed by the time $(t_2 - t_1)$ needed for the perturbed wavefront to travel from one pupil to another, which produces in the frequency domain a phase term equal to

$$\varphi(\nu) = 2\pi \;(t_2 - t_1)\; \nu. \tag{27}$$

From Fig. 6 one can easily calculate the time $t_2 - t_1$ and introduce it in last equation to obtain:

$$\varphi(\nu) = 2\pi \;\frac{B\cos(\eta-\gamma)}{v}\; \nu. \tag{28}$$

When $(\eta-\gamma) > 90^o$,$\varphi(\nu)$ has a negative slope because the turbulent structures go from P_2 to P_1.

One can notice that expression (28) is equal to the argument of the phase factor in Eq. (26), expressed in the exponential term outside the integral. The phase term $\varphi(\nu)$ is not exactly equal to the phase of $W_{\alpha,\mathbf{B}}(\nu)$. The integral in Eq. (26) can be seen as the Fourier Transform of a function of q that is not even because of the first factor $\left[\left(\frac{\nu}{v}\cos\eta - q\sin\eta\right)^2\right]$, producing a non-zero imaginary part of the integral result. This factor comes from the particular direction of the AA fluctuations that provokes an anisotropy in the AA spatial spectrum. Indeed, the AA spatial spectrum is a product of the spatial spectrum of the wavefront phase, that is isotropic, multiplied by one component of the spatial frequency squared[40]. However, the contribution of this integral to the total TCS phase is weak, limited to low frequencies, and noticeable only for some parameter combinations. For instance, in the case of $\eta = \gamma = 0$, the phases for 3 different values of B, represented in Fig. 7-b, are exactly given by Eq. (28). Almost the same behavior is found in Fig. 9-b, that represents the TCS phase for 3 different values of the baseline angle γ, and $B = 1m$, $\eta = 0$. As the wind velocity angle η becomes higher, the contribution of the above mentioned integral to the total phase can be noticeable, as shown in Fig. 10-b in which the TCS phase is represented for 3 different values of η, the other parameters being fixed. In the case of $\eta = 45^o$, at low frequencies the total phase (full line) diverges from $\varphi(\nu)$ (dashed line), but at higher frequencies both lines have the same slope. As explained in section 5B, the measurement of this slope leads to the wind velocity vector. No influence of the wavefront outer scale on the TCS phase has been noticed, as testified in Fig. 11-b.

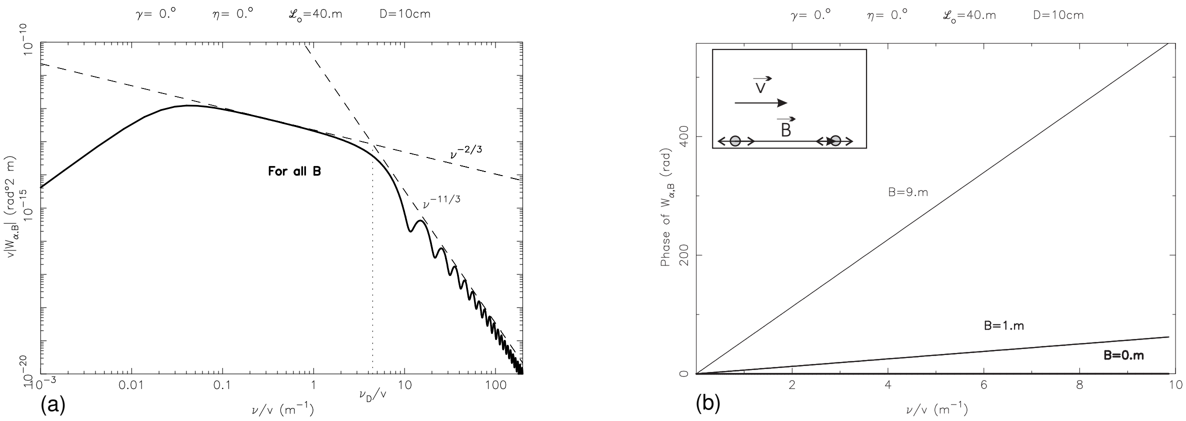

Fig. 7. Influence of the baseline separation on the Angle of Arrival (AA) Temporal Cross-Spectrum (TCS). The TCS modulus multiplied by the wind speed (a) and the TCS phase (b) are represented as functions of ν/v, for 3 values of B, other parameters beeing fixed to the values shown. The scheme in the frame in (b) represents the orientations of the mean wind velocity, the baseline vector (between 2 circular pupils), and the AA fluctuations (arrows on pupils). Wind velocity and baseline are parallel to each other in which case the TCS modulus (a) equals the AA temporal power spectrum for all B. Power laws and high frequency cut-off are shown. In (b) are represented the total phase as well as the phase contribution $\varphi(\nu)$ (Eq.(28)), that are exactly superimposed for each values of B.

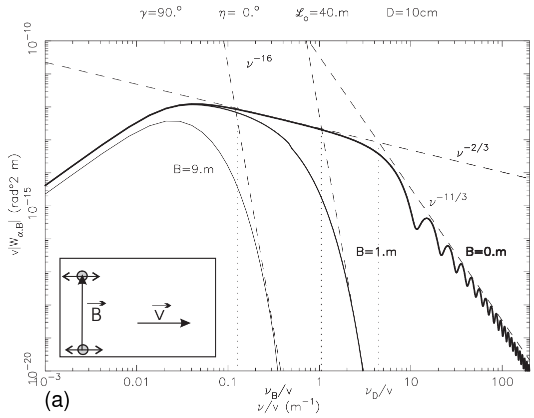

Fig. 8. Similar to Fig. 7, but with wind velocity and baseline perpendicular to each other in which case the TCS phase is equal to 0 for all B, thus it is not represented.

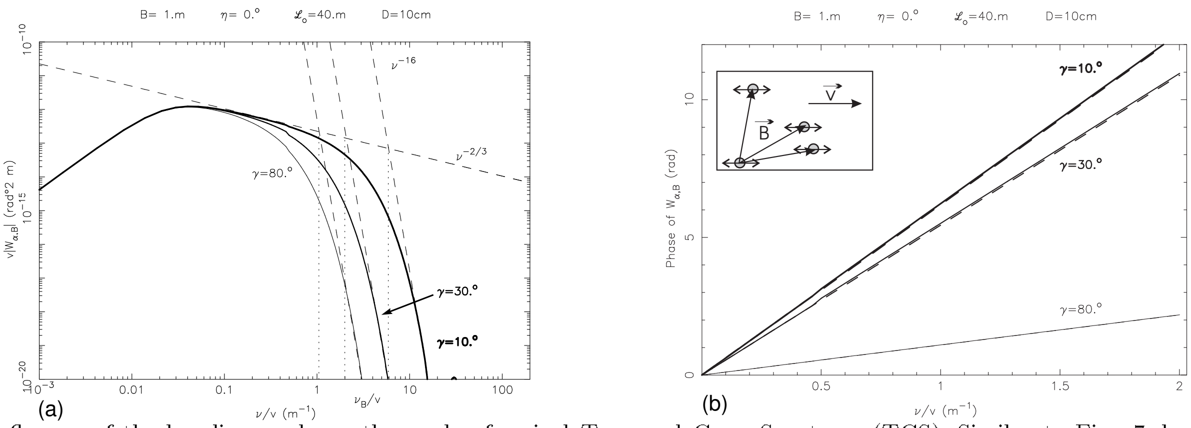

Fig. 9. Influence of the baseline angle on the angle of arrival Temporal Cross-Spectrum (TCS). Similar to Fig. 7, but the TCS modulus (a) and phase (b) are shown for 3 values of the baseline angle γ. Dashed lines in (b) represent the phase contribution $\varphi(\nu)$ (Eq.(28)), which are almost superimposed to the total phase (continuous line) for $\gamma = 10^o$ and $\gamma = 30^o$, and exactly superimposed for $\gamma = 80^o$.

Three characteristic frequencies can be identified for the TCS modulus. There is a frequency cut-off that is a consequence of a finite wavefront outer scale, given approximately by

$$\nu_{\mathcal{L}_0} \sim \frac{v}{\mathcal{L}_0}. \tag{29}$$

It defines a low-frequency domain for $\nu \leq \nu_{\mathcal{L}_0}$. It appears in all the TCS modulus plots presented, but for simplicity reasons only in Fig. 11-a this cut-off frequency is shown explicitly, for different values of $\mathcal{L}_0$. Another feature is produced by the baseline component in the direction perpendicular to the wind. It is manifested as a second frequency cut-off

$$\nu_B \simeq \frac{v}{|\overrightarrow{CP_2}|} = \frac{v}{B\sin(\ |\eta - \gamma|\ )}. \tag{30}$$

As it is generally expected that the projection of the baseline in the direction perpendicular to the wind ($B\sin(\ |\eta-\gamma|\ )$) is less than $\mathcal{L}_0$, ν_B appears at higher frequencies than $\nu_{\mathcal{L}_0}$, allowing the definition of middle and high-frequency domains: $\nu_{\mathcal{L}_0} \leq \nu \leq \nu_B$ and $\nu_B \leq \nu$, respectively. Fig. 9-a represents the TCS modulus for different values of the baseline angle γ, showing ν_B explicitely. It is empirically found that in the middle frequency domain the TCS modulus follows a $\nu^{-2/3}$ power law (encountered also in the AA power spectrum), and that at high frequencies the TCS modulus tends approximately to a ν^{-16} power law. These power laws are represented by straight lines with the corresponding slopes, and tangent to the TCS modulus curve. Note that the value of the cutt-off frequency ν_B defined by Eq. (30) corresponds very precisely to the abscissa of the intersection point of the straight lines representing the power laws, for all the parameter-value combinations in which this cutt-off frequency is present.

When $B\sin(\ |\eta-\gamma|\ )$ becomes smaller than the pupil diameter, the TCS modulus equals the AA power spectrum. The high frequency cut-off is then dominated by the pupil filtering, and is estimated by

$$\nu_D \simeq 0.5\frac{v}{D}, \tag{31}$$

in which case the middle and the high-frequency domains are rather defined by $\nu_{\mathcal{L}_0} \leq \nu \leq \nu_D$ and $\nu_D \leq \nu$ respectively. Fig. 7-a shows an example of such a case, for 3 different B, and $\eta = \gamma = 0$. The curves are exactly superimposed because the baseline and the wind are in the same direction ($\eta - \gamma = 0$), implying that $B\sin(\ |\eta-\gamma|\ ) = 0$ for all B. At high frequency a $\nu^{-11/3}$ power law is found. The graphical procedure for determining the cut-off frequency ν_D is analogous to the one employed in the case of ν_B. Conan *et al.*[33] found the same high frequency power law for the AA power spectrum with an infinite outer scale, but they estimated the corresponding cut-off frequency to be near $0.3(\nu/D)$. The difference between this expression and Eq. (31) comes from the graphical procedure used for identifying the cut-off frequency. Fig. 10-a represents the influence of the wind velocity angle

η on the TCS modulus. It includes another example of an AA power spectrum for the case $\eta = \gamma$. For the other two values of η, one can notice the high frequency cut-off ν_B and the ν^{-16} power law explained below. When η gets close to 90^o, a valley appears in the middle-frequency range. This feature is independent of the baseline angle. It depends on the angle η between the AA measurement direction and the wind velocity. In the low frequency range, the relative amount of energy increases as η increases. This influence of η makes it impossible to establish a power law behavior at low frequencies. This is why the cut-off frequency $\nu_{\mathcal{L}_0}$ has not been graphically determined like ν_B and ν_D. A more complicated model would be necessary for establishing a precise graphical method of determination of $\nu_{\mathcal{L}_0}$.

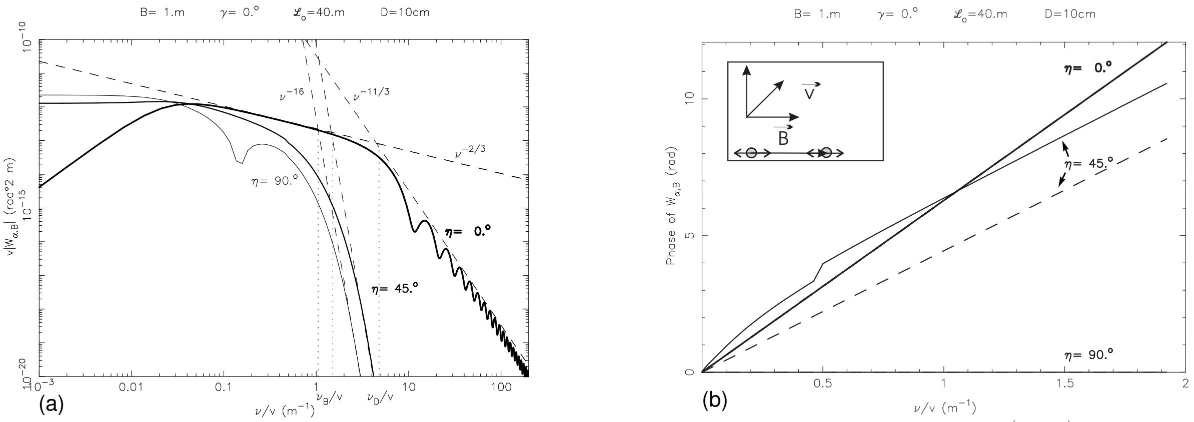

Fig. 10. Influence of the mean wind velocity angle on the angle of arrival Temporal Cross-Spectrum (TCS). Similar to Fig. 7, but the TCS modulus (a) and phase (b) are shown for 3 values of the mean wind velocity angle η. Dashed line in (b) represents the phase contribution $\varphi\,(\nu)$ (Eq.(28)), for $\eta = 45^o$. For the 2 other values of η this contribution appears superimposed to the total phase, represented in continuous lines.

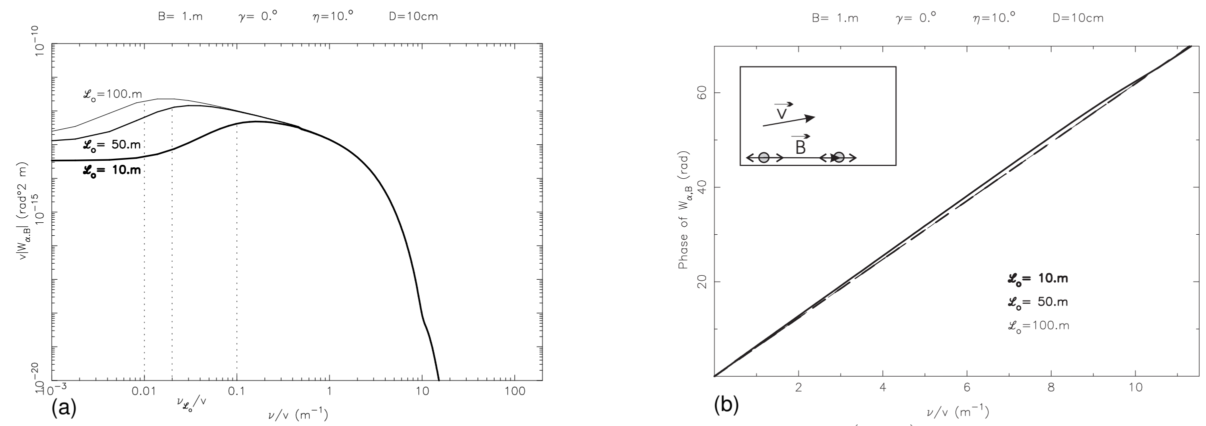

Fig. 11. Influence of the outer scale on the angle of arrival Temporal Cross-Spectrum (TCS). Similar to Fig. 7, but the TCS modulus (a) and phase (b) are shown for 3 values of the outer scale $\mathcal{L}_0$. Low frequency cut-offs are shown. No significative influence on the TCS phase is noticed.

5. DISCUSSION: EXPERIMENTAL POSSIBILITIES

A. Estimation of the 2-D normalized covariance

Takato &Yamaguchi[22] gave an analytical expression of the spatial correlation of Zernike phase-expansion coefficients with finite outer scale. It includes the correlation of the tilt, which is equivalent to the AA in one direction. As declared by the authors, the calculation is easier by numerical integration than using the formula obtained. They also concluded that the experimental tip and tilt correlations obtained at Keck telescope[41] do not fit well to theoretical curves because the data are biased by mechanical vibrations. In order to avoid these problems, the normalized covariance of the AA, defined by Eq. (17), is experimentally determined in the following way using the GSM experiment:

The covariance in the numerator of Eq. (17) is estimated from measurements obtained using mechanically independent modules, having different resonance frequencies from each other. Vibrations of both modules can be considered as statistically independent processes. Tracking errors are negligible because the measurement direction of the AA is kept perpendicular to the tracking direction. For these reasons the covariance of AA induced by vibrations and tracking errors can be different from zero only because of statistical errors, not affecting significantly the covariance of the turbulence-induced AA. Measurements used to calculate the structure function in the denominator of Eq. (17) are obtained from two modules solidly coupled to the same mounting, forming a baseline of about 30 cm. Vibrations and tracking errors are identical in each module, and they cancel out when calculating the structure function. Takato &Yamaguchi[22] proposed to measure tip and tilt structure functions and normalize them by the values obtained with the smallest baseline, using a Shack-Hartmann sensor on a single telescope.

B. Temporal cross spectrum

The TCS is a very complete statistical tool as it contains temporal as well as spatial information on the random process under study (AA in this case). Usually, the theoretical temporal characterization of the wavefront, perturbed by the atmospheric turbulence, is established calculating exclusively temporal power spectra of the AA or any other modal component[12–17,27,31–33]. An advantage of the AA TCS, in this theoretical study, is that one can identify the mean wind direction in addition to the parameters obtainable from the power spectra (v, r_0, $\mathcal{L}_0$). The most convinient method, as shown below, is to determine the slopes of $\varphi(\nu)$, Eq. (28), from the TCS phase in its linear region, for two known baselines having different angles γ. This gives two independent linear equations from which the mean wind velocity vector (v and η) can be determined. The simplest way is to choose $\gamma = 0^o$ for one of the baselines and $\gamma = 90^o$ for the other, both with the same modulus B. In principle, v and η may also be deduced from the estimation of the cutt-off frequency ν_B in the TCS modulus, as suggested by Eq. (30). However, determining ν_B implies to be able to detect the ν^{-16} power law. This appears to be beyond the possibilities offered by any measurement because the expected noise at high frequencies would drastically limit the dynamic range making impossible to reach the asymptotic behavior. A third method consisting of the measurement of both TCS modulus and phase would lead to the same experimental difficulties. An eventual solution to this problem could be a modelisation of the TCS modulus in the middle frequency domain with ν_B/v as a parameter. Nevertheless, Eq. (30) contains an absolute value which brings an ambiguity in the determination of η.

The TCS model given here assumes the "frozen turbulence" hypothesis. Gendron & Lena[42] have published experimental evidence of the validity of this hypothesis for baselines up to the telescope diameter they used (3.6m). This leads us to suppose that the TCS model is valid for short baselines, although we are convinced that this model has to serve as a basis for more detailed models including, in the order of importance, multiple turbulent layers, variations in the wind velocity, and unfrozen turbulence. In the case of multiple layers, the TCS of the AA at pupils on the ground is equal to the sum of the TCS of the AA induced by each layer, assumed to be statistically independent of each other. However, the behavior of modulus and phase of the resulting TCS is not straightforward, because each individual TCS is a complex quantity. The expected effect of variations in the wind velocity, for the single layer case, is to affect mainly the TCS modulus at high temporal frequencies, whereas a failure of the "frozen turbulence" hypothesis would rather affect principally low frequencies, because at the corresponding long time intervals there would be significant evolution of the turbulence, as already outlined by Davis *et al.*[11]. Each of the three situations just mentioned needs specific investigations, which are beyond the scope of this paper.

C. Determination of $\mathcal{L}_0$

There are arguments in favor and against the variability of $\mathcal{L}_0$ values reported in the literature (Table 1). It should not be forgotten that the wavefront outer scale can depend on the site, and on seeing conditions. If thin optical turbulent layers in the free atmosphere[8] were systematically confirmed, one would expect that the contribution for large $\mathcal{L}_0$ values would come from the boundary layer. On the other hand, one can notice that largest outer scales reported were obtained from measurements of the temporal phase power spectrum assuming the "frozen turbulence" model in its interpretation. Disagreement between spatial phase structure function at long baselines and temporal phase power spectrum at very low frequency, when compared using such a model has been reported[15]. Estimation of $\mathcal{L}_0$ from temporal power spectra suffers strongly if the "frozen turbulence" hypothesis fails because the signature of $\mathcal{L}_0$ occurs at very low frequencies. Our understanding of the effect of turbulence at baselines near the wavefront outer scale needs further work, especially concerning the temporal evolution. For these reasons we decided to estimate the wavefront outer scale from the spatial AA covariances measured with several baselines, which has been the leading idea in designing the Grating Scale Monitor[38, 23], instead of exploiting the cut-off frequency $\nu_{\mathcal{L}_0}$of the AA TCS modulus, expressed in Eq. (29). The theoretical model of the spatial 2-D covariance of the AA fluctuations do not assume any temporal behavior, as for instance the "frozen turbulence" hypothesis. The only condition in the experimental estimation is to measure the AA simultaneously at both pupils during an exposure time sufficiently short to admit that the turbulence do not evolve at all. In the specific case of GSM experiment the effective exposure time is 5 ms. Until now, interferometric techniques cannot achieve multiple simultaneous baselines making difficult a purely spatial analysis for determining $\mathcal{L}_0$, which explains the repeatedly reported phase temporal power spectrum measurements for that same goal.

6. SUMMARY

Theoretical calculation and analysis of the 2-D covariance and TCS of the AA fluctuations induced by atmospheric turbulence have been presented. This theoretical work was inspired by the data analysis that will be performed with the Grating Scale Monitor AA measurements. Great attention was paid to the wavefront outer scale $\mathcal{L}_0$, introduced by means of the Von Kàrmàn phase spectrum, with an infinitely small inner scale. Both results apply for any baseline vector in the mean wavefront plane. The AA TCS was calculated considering that the wavefront is carried by the wind without deformation with a mean velocity $\mathbf{v}$, for times greater or of the order of $\mathcal{L}_0/|\mathbf{v}|$. A method for obtaining experimental 2-D normalized covariance of AA that avoids bias introduced by possible mechanical vibrations, and that takes correctly into account the effect of the wavefront outer scale, consists of dividing the covariance of AA measured with mechanically uncoupled devices, by the structure function of AA measured with mechanically coupled devices, both measurements being synchronized. Fitting experimental AA normalized covariance to the theoretical model presented here allows retrieval of the wavefront outer scale. Fried parameter r_0 can also be estimated from the same AA structure function measurements. The behavior of the AA TCS modulus at temporal frequencies lower than the cut-off imposed by the outer scale is similar to the behavior of the AA temporal power spetrum. The baseline component in the wind direction influences the slope of the TCS phase, whereas the component in the perpendicular direction defines cut-off frequencies in the TCS modulus. When the projection of the baseline in the direction perpendicular to the wind is smaller than the pupil size the AA TCS modulus equals the AA temporal power spectrum. It was shown that from slopes of TCS phases obtained with at least 2 baselines not parallel to each other, one can calculate the mean speed as well as the mean direction of the wind. The coherence time of the wavefront can be evaluated from Fried parameter r_0 and the mean wind speed[15]. We prefer not to try to determine $\mathcal{L}_0$ from the AA TCS, because strong uncertainties remain in the validity of Taylor hypothesis for long baselines. Results presented here concerning the AA TCS are valid for a "frozen turbulence", and should serve as a basis for further work towards a multi-layer model. Further investigations are to be undertaken for satisfactory model of the temporal behavior of the wavefront at baselines greater than the outer scale.

---

1. J. Borgnino, "Estimation of the spatial coherence outer scale relevant to long baseline interferometry and imaging in optical astronomy," Appl. Opt. **29**, 1863-1865 (1990).
2. C.E. Coulman, J. Vernin, Y. Coqueugniot, and J.L. Caccia, "Outer scale of turbulence appropriate to modeling refractive-index structure profiles," Appl. Opt. **27**, 155-160 (1988).

3. R.R. Beland, and J.H. Brown, "A deterministic temperature model for stratospheric optical turbulence," Physica Scripta. **37**, 419-423 (1988).
4. C.E. Coulman, "Vertical profiles of small-scale temperature structure in the atmosphere," Boudary-layer meteorol. **4**, 169 (1973).
5. J.L. Bufton, "Comparison of vertical profile turbulence structure with stellar observations," Appl. Opt. **12**, 1785-1793 (1973).
6. R. Barletti, G. Ceppatelli, L. Paternò, A. Righini, and N. Speroni, "Daytime r_0 evaluated from vertical microthermal measurements," Appl. Opt. **16**, 2419-2421 (1977).
7. F. Delaudier, D. Sidi, M. Crochet, and J. Vernin, "Direct evidence of 'sheets' in the atmospheric temperature field," J. Atmos. Sci. **51**, 237-248 (1994).
8. C.E. Coulman, J. Vernin, and A. Fuchs, "Optical seeing-mechanism of formation of thin turbulent laminae in the atmosphere," Appl. Opt. **34**, 5461-5474 (1995).
9. A. Fuchs, "Contribution à l'étude de l'apparition de la turbulence optique dans les couches minces. Concept du SCIDAR généralisé," Thèse de doctorat (Université de Nice, France) (1995).
10. J.M. Mariotti, and G.P. Di Benedetto, "Pathlength stability of synthetic aperture telescopes: the case of the 25 cm CERGA interferometer," in *Very Large Telescopes, their Instrumentation and Programs,* M.H. Ulrich, and K. Jear eds. (European Southern Observatory Garching Germany), Proc. IAU colloq. **79**, 257-265 (1984).
11. J. Davis, P.R. Lawson, A.J. Booth, W.J. Tango, and E.D. Thorvaldson, "Atmospheric path variations for baselines up to 80 m measured with the Sidney University Stellar Interferometer," Mon. Not. R. Astron. Soc. **277**, L53-L58 (1995).
12. N.S. Nightingale, and D.F. Buscher, "Interferometric seeing measurements at the La Palma Observatory," Mon. Not. R. Astr. Soc. **251**, 155-166 (1991).
13. C.A. Haniff, J.E. Baldwin, P.J. Warner, and T.R. Scott, "Atmospheric phase fluctuation measurements: interferometric results from the WHT and COAST telescopes," in *Amplitude and Intensity Spatial Interferometry II,* J.B. Breckinridge, ed., Proc. Soc. Photo-Opt. Instrum. Eng. **2200**, 407-417 (1994).
14. M. M. Colavita, M. Shao, and D. H. Staelin, "Atmospheric phase measurements with the Mark III stellar interferometer," Appl. Opt. **26**, 4106-4112 (1987).
15. D.F. Buscher, J.T. Amstrong, C.A. Hummel, A. Quirrenbach, D. Mozurkewich, K.J. Johnston, C.S. Denison, M. M. Colavita, and M. Shao, "Interferometric seeing measurements on Mt. Wilson: power spectra and outer scales," Appl. Opt. **34**, 1081-1096 (1995).
16. D.F. Buscher, J.T. Armstrong, D. Mozurkewich, and C.S. Denison, "Atmospheric fluctuation measurements with the MKIII interferometer and the power spectra of everything," in *High Resolution Imaging by Interferometry II,* J.M. Beckers, and J.M. Merkle eds. (European Southern Observatory Garching Germany), Proc. ESO conf. **39**, 1029-1038 (1991).
17. M. Bester, W. C. Danchi, C. G. Degiacomi, L.J. Greenhill, and C.H. Townes, "Atmospheric fluctuations: empirical structure functions and projected performances of future instruments," Astrophysical Journal **392**, 357-374 (1992).
18. Ph. Berio, D. Mourard, F. Vakili, J. Borgnino, and A. Ziad, "Effects of atmospheric spectral decorrelation on visibility measurements in Michelson interferometry," J. Opt. Soc. Am. **14**, 114-121 (1997).
19. M. Tallon, "Contributions à l'imagerie à Haute Résolution Angulaire: analyse de la surface d'onde, source laser de référence, optique adaptative," Thèse de doctorat (Université de Nice, France) (1989).
20. F. Rigaut, G. Rousset, P. Kern, J.C. Fontanella, J.P. Gaffard, F. Merkle, and P. Lena "Adaptive optics on a 3.6m telescope: results and performance," Astron. Astrophys. **250**, 280-290 (1991).
21. A. Ziad, J. Borgnino, F. Martin, and A. Agabi, "Experimental estimation of the spatial-coherence outer scale from a wavefront statistical analysis," Astron. Astrophys. **282**, 1021-1033 (1994).
22. N. Takato, and I. Yamaguchi, "Spatial correlation of Zernike phase-expansion coefficients for atmospheric turbulence with finite outer scale," J. Opt. Soc. Am. **12**, 957-965 (1995).
23. A. Agabi, J. Borgnino, F. Martin, A. Tokovinin, and A. Ziad, "G.S.M.: a Grating Scale Monitor for atmospheric turbulence measurements. II. First measurements of the wavefront outer scale at the O.C.A.," Astron. Astrophys. *Suppl. Ser.* **109**, 557-562 (1995).
24. A. Ziad, J. Borgnino, A. Agabi, and F. Martin, "Optimized spectral bandwidth in high angular resolution imaging, effect of a finite spatial-coherence outer scale," Experimental Astronomy **5**, 247-268 (1994).
25. A. Ziad, "Estimation des échelles limites de cohérence spatiale des fronts d'onde et optimisation des observations à Haute Résolution Angulaire en Astronomie," Thèse de doctorat (Université de Nice, France) (1993).
26. D.M. Winker, "Effect of a finite outer scale on the Zernike decomposition of atmospheric optical turbulence," J. Opt. Soc. Am. **8**, 1568-1573 (1991).
27. V.V. Voitsekhovich, and S. Cuevas, "Adaptive optics and the outer scale of turbulence," J. Opt. Soc. Am. **12**, 2523-2531 (1995).

28. G. Boreman, and C. Dainty, "Zernike expansions for non-Kolmogorov turbulence," J. Opt. Soc. Am. **13**, 517-522 (1996).
29. F. Roddier, J. M. Gilli, and G. Lund, "On the origin of speckle boiling and its effects in stellar speckle interferometry," J. Optics (Paris) **13**, 263-271 (1982).
30. F. Roddier, and P. Lena "Long-baseline michelson interferometry with ground-based telescopes operating at optical wavelengths," J. Optics (Paris) **15**, 171-182 (1984).
31. C. Aime, J. Borgnino, F. Martin, R. Petrov, and G. Ricort, "Contribution to the space-time study of stellar speckle patterns," J. Opt. Soc. Am. **3**, 1001-1009 (1986).
32. F. Roddier, M.J. Northcott, J.E. Graves, and D.L. McKenna, "One-dimensional spectra of turbulence-induced Zernike aberrations: Time-delay and isoplanicity error in partial adaptive compensation," J. Opt. Soc. Am. **10**, 957-965 (1993).
33. J.-M. Conan, G. Rousset, and P.-Y. Madec, "Wave-front temporal spectra in high-resolution imaging through turbulence," J. Opt. Soc. Am. **12**, 1559-1570 (1995).
34. P.-Y. Madec, J.-M. Conan, and G. Rousset, "Temporal characterisation of atmospheric wavefront for adaptive optics," in *Progress in Telescopes and Instrumentation Technologies,* M.-H. Ulrich ed. (European Southern Observatory Garching Germany), Proc. ESO conf. **42**, 471-474 (1992).
35. G. Rousset, P.-Y. Madec, and D. Rabaud, "Adaptive optics partial correction simulation for two telescope interferometry," in *High Resolution Imaging by Interferometry II,* J.M. Beckers, and J.M. Merkle eds. (European Southern Observatory Garching Germany), Proc. ESO conf. **39**, 1095-1104 (1991).
36. H.M. Martin, "Image motion as a measure of seeing quality," Publ. Astron. Soc. Pac. **99**, 1360-1370 (1987).
37. B. Lopez, "How to monitor optimum exposure times for high resolution imaging modes?," Astron. Astrophys. **253**, 635-640 (1992).
38. F. Martin, A. Tokovinin, A. Agabi, J. Borgnino, and A. Ziad, "G.S.M.: a Grating Scale Monitor for atmospheric turbulence measurements. I. The instrument and first results of angle of arrival measurements," Astron. Astrophys. *Suppl. Ser.* **108**, 173-180 (1994).
39. F. Roddier, "The effects of atmospheric turbulence in optical astronomy," in *Progress in Optics*, E. Wolf, ed. (North-Holland, Amsterdam) Vol. **19**, 281-376 (1981).
40. J. Borgnino, F. Martin, and A. Ziad, "Effect of a finite outer scale on the covariances of angle-of-arrival fluctuations," Opt. Com. **91**, 267 (1992).
41. F. Dekens, D. Kirkman, G. Chanan, T. Mast, J. Nelson, G. Illingworth, and P. Wizinowich, "High speed seeing measurements at Keck telescope," in *Adaptive Optics in Astronomy,* M.A. Ealey, ed., Proc. Soc. Photo-Opt. Instrum. Eng. **2201**, 310-313 (1994).
42. E. Gendron, and P. Lena, "Single layer atmospheric turbulence demonstrated by adaptive optics observations," Astrophys. and Space Science **239**, 221-228 (1996).